

ARTICLE

DOI: 10.1038/s41467-018-04660-4

OPEN

Double thermoelectric power factor of a 2D electron system

Yuqiao Zhang¹, Bin Feng², Hiroyuki Hayashi³, Cheng-Ping Chang⁴, Yu-Miin Sheu^{4,5}, Isao Tanaka³, Yuichi Ikuhara² & Hiromichi Ohta^{1,6} 

Two-dimensional electron systems have attracted attention as thermoelectric materials, which can directly convert waste heat into electricity. It has been theoretically predicted that thermoelectric power factor can be largely enhanced when the two-dimensional electron layer is far narrower than the de Broglie wavelength. Although many studies have been made, the effectiveness has not been experimentally clarified thus far. Here we experimentally clarify that an enhanced two-dimensionality is efficient to enhance thermoelectric power factor. We fabricated superlattices of [*N* unit cell SrTi_{1-x}Nb_xO₃][11 unit cell SrTiO₃]₁₀—there are two different de Broglie wavelength in the SrTi_{1-x}Nb_xO₃ system. The maximum power factor of the superlattice composed of the longer de Broglie wavelength SrTi_{1-x}Nb_xO₃ exceeded $\sim 5 \text{ mW m}^{-1} \text{ K}^{-2}$, which doubles the value of optimized bulk SrTi_{1-x}Nb_xO₃. The present approach—use of longer de Broglie wavelength—is epoch-making and is fruitful to design good thermoelectric materials showing high power factor.

¹Graduate School of Information Science and Technology, Hokkaido University, N14W9, Kita, Sapporo 060–0814, Japan. ²Institute of Engineering Innovation, The University of Tokyo, 2–11–16 Yayoi, Bunkyo, Tokyo 113–8656, Japan. ³Department of Materials Science and Engineering, Kyoto University, Yoshida-Honmachi, Sakyo, Kyoto 606–8501, Japan. ⁴Department of Electrophysics, National Chiao Tung University, 1001, University Rd, Hsinchu 30010, Taiwan. ⁵Center for Emergent Functional Matter Science, National Chiao Tung University, Hsinchu 30010, Taiwan. ⁶Research Institute for Electronic Science, Hokkaido University, N20W10, Kita, Sapporo 001–0020, Japan. Correspondence and requests for materials should be addressed to H.O. (email: hiromichi.ohta@es.hokudai.ac.jp)

Currently, more than 60% of the energy produced from fossil fuels is lost as waste heat. Thermoelectric energy conversion, which is the process where waste heat is transformed into electricity by the Seebeck effect, is attracting attention as a potential energy harvesting technology^{1–4}. The performance of thermoelectric materials is generally evaluated in terms of a dimensionless figure of merit,

$$ZT = S^2 \cdot \sigma \cdot T \cdot \kappa^{-1}, \quad (1)$$

where Z is the figure of merit, T is the absolute temperature, S is the thermopower (Seebeck coefficient), σ is the electrical conductivity, and κ is the sum of the electronic (κ_{ele}) and lattice thermal conductivities (κ_{lat}) of a thermoelectric material.

There are two strategies to improve ZT of a thermoelectric material. One is to reduce κ_{lat} . Recently, state-of-the-art nanostructuring techniques have reduced κ_{lat} significantly through phonon scattering by nanosized structural defects^{5–8}. Such techniques have realized high-performance thermoelectric materials with a large ZT of 1.5–2. The other strategy is an enhancement of the product $S^2 \cdot \sigma$, which is called power factor (PF). However, it is extremely difficult to enhance PF due to the trade-off relationship between S and the carrier concentration (n). Therefore, PF has a local maximum value in three-dimensional (3D) bulk systems.

In a two-dimensional electron system (2DES) such as metal/insulator superlattices, electron carriers are confined within a thin layer (thickness thinner than the de Broglie wavelength, λ_D). 2DES is an efficient strategy to achieve an enhanced PF. The effectiveness of 2DES was theoretically predicted by Hicks and Dresselhaus⁹; 2DES in extremely narrow layers exhibits an enhanced S without reducing σ because the density of states (DOS) near the bottom of the conduction band increases as the 2DES layer thickness decreases. These layers are narrower than the λ_D ,

$$\lambda_D = \frac{h}{\sqrt{3 \cdot m^* \cdot k_B \cdot T}}, \quad (2)$$

where h , m^* , and k_B are Planck's constant, effective mass of conductive electron or hole, and Boltzmann constant, respectively^{9–13}.

Many experimental studies have been made to clarify the effectiveness of 2DES to enhance PF using PbTe/Pb_{1–x}Eu_xTe multiple-quantum-well¹⁰, electron-doped SrTiO₃-based superlattices^{14,15},

SiGe-based superlattices^{16,17}, and Bi₂Te₃-based superlattices¹⁸. These 2DES layers showed enhanced S . However, total enhancement of PF was very small because of the insulator layer thickness. Thus, the effectiveness of 2DES has not been experimentally clarified thus far.

Here we experimentally clarify that an enhanced two-dimensionality is efficient to improve thermoelectric PF. We fabricated superlattices of [N unit cell SrTi_{1–x}Nb_xO₃]/[11 unit cell SrTiO₃]₁₀—there are two different de Broglie wavelength in the SrTi_{1–x}Nb_xO₃ system. The maximum PF of the superlattice composed of the longer de Broglie wavelength SrTi_{1–x}Nb_xO₃ exceeded $\sim 5 \text{ mW m}^{-1} \text{ K}^{-2}$, which doubles the value of optimized bulk SrTi_{1–x}Nb_xO₃. The present approach—use of longer de Broglie wavelength—is epoch-making and is fruitful to design good thermoelectric materials showing high PF.

Results

Hypothesis. In order to enhance total PF of 2DES, two-dimensionality should be enhanced. Use of longer λ_D should be effective if the electron carriers are confined within a defined thickness layer (Fig. 1). Very recently, we observed a steep decrease in m^*/m_e at $x \sim 0.3$ in SrTiO₃–SrNbO₃ solid solution system, SrTi_{1–x}Nb_xO₃ (x is ranging from 0.05 to 0.9; Fig. 2)¹⁹. The ratio x of SrTi_{1–x}Nb_xO₃ can be divided into two regions, region A (x is <0.3) and region B (x is >0.3). The origin of the two regions is most likely due to the difference in the overlap population between the Ti 3*d* and Nb 4*d* orbitals ($r_{\text{Ti}3d}$ is 48.9 pm and $r_{\text{Nb}4d}$ is 74.7 pm)²⁰. We calculated λ_D values of SrTi_{1–x}Nb_xO₃ using the Eq. (2). The λ_D value in region B is ~ 5.3 nm, which is 27% longer than that in region A (~ 4.1 nm). One can expect that S -enhancement factor in region B is much higher than that in region A because of higher two-dimensionality. Therefore, we hypothesized that SrTi_{1–x}Nb_xO₃-based 2DES can be used to clarify the effectiveness of 2DES to enhance PF experimentally.

We fabricated [N uc SrTi_{1–x}Nb_xO₃]/[11 uc SrTiO₃]₁₀ superlattices (N is ranging from 1 to 12, x is ranging from 0.2 to 0.9) by a pulsed laser deposition (PLD) technique on insulating (001) LaAlO₃ (pseudo-cubic perovskite, the lattice parameter, a is 3.79 Å) single-crystal substrates using dense ceramic disks of a SrTiO₃–SrNbO₃ mixture and SrTiO₃ single crystal as the targets. The thicknesses of different layers were monitored in situ using the intensity oscillation of the reflection high-energy electron diffraction (RHEED) spots. (See Experimental Section.) High-

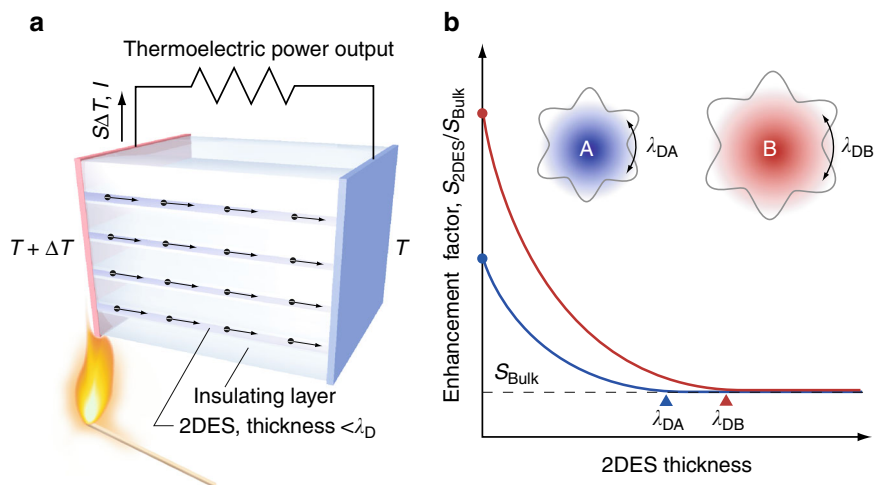


Fig. 1 Thermoelectric effect of a 2D electron system. **a** Schematic illustration of thermoelectric Seebeck effect in a 2DES. A thermoelectric power output ($S \cdot \Delta T \cdot I$) can be obtained when ΔT is introduced. **b** The hypothesis that a 2DES with longer de Broglie wavelength (λ_D) shows a larger enhanced factor of thermopower

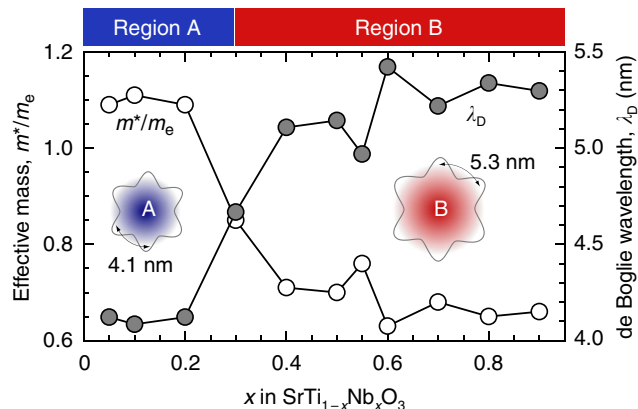


Fig. 2 SrTiO₃-SrNbO₃ solid solution: a model system having two different λ_D . x -dependent effective mass (m^*/m_e , white symbols) and λ_D (gray symbols) for SrTi_{1-x}Nb_xO₃ solid solutions. m^*/m_e exerts a decreasing tendency with x , resulting in an increased λ_D . Sharp changes in both m^*/m_e and λ_D are detected around $x = 0.3$ due to the conduction band transition from Ti 3d to Nb 4d. The properties of SrTi_{1-x}Nb_xO₃ solid solutions can be divided into two regions based on the conduction bands (Ti 3d \rightarrow region A and Nb 4d \rightarrow region B). Inset: schematic illustrations of conduction electrons at regions A and B. At region B, λ_D is ~ 5.3 nm, while it is ~ 4.1 nm at region A

resolution X-ray diffraction (XRD) measurements revealed that the resultant superlattices were heteroepitaxially grown on (001) LaAlO₃ with cube-on-cube epitaxial relationship with superlattice structure. Atomically smooth surfaces with stepped and terraced structure were observed by an atomic force microscopy (AFM).

Microstructure and electronic structure. Figure 3a summarizes the atomic arrangements of the [1 uc SrTi_{0.4}Nb_{0.6}O₃][11 uc SrTiO₃]₁₀ superlattice. Rather bright bands are observed near each SrTi_{0.4}Nb_{0.6}O₃ layer in the Cs-corrected high-angle annular dark-field scanning transmission electron microscopy (HAADF-STEM) image. In the magnified image, the #4 atom in the B-site column is brighter than the nearby atoms. However, there is no obvious difference in the A-site column, indicating Nb substitution occurs for the #4 atom in the B-site column. The electron energy loss spectroscopy signal of #4 is broader than that of the nearby atoms, implying the coexistence of Ti⁴⁺/Ti³⁺ in the SrTi_{0.4}Nb_{0.6}O₃ layers²¹. Therefore, in our superlattice fabrication, Nb ions are successfully confined into 1 uc of SrTi_{0.4}Nb_{0.6}O₃ layers²².

In order to clarify the 2DES formation, the electronic band structures of the [1 uc SrNbO₃][10 uc SrTiO₃] superlattices were calculated based on the projector-augmented wave (PAW) method (Fig. 3b). The E_F is located on the higher-energy side of the conduction band minimum for the first and second nearest-neighbor SrTiO₃ layers (Ti first NN and Ti second NN) together with the 1 uc SrNbO₃ layer (Nb). The electron carriers can seep from the SrNbO₃ layers into the SrTiO₃ layer. Delugas et al.²³ have also predicted theoretically that for lower Nb substituted samples, it is much easier for the electrons, especially in the d_{xz} and d_{yz} bands, to spread out to the neighboring SrTiO₃ layers, reducing the two-dimensionality. However, as the Nb content increases, the minimum thickness of the barrier layer may be reduced to 5 uc in the SrNbO₃ case. There is no doubt that the electron diffusion cannot be removed thoroughly in superlattice structure, but diffusion effects can be effectively suppressed by the high Nb substitution. From the band calculation, 2DES in our work is mainly confined to the 1 uc

SrTi_{1-x}Nb_xO₃ layers and should contribute to the S enhancement.

In order to further confirm the superlattice structure, we measured the κ of the [1 uc SrTi_{0.4}Nb_{0.6}O₃][11 uc SrTiO₃]₁₀ superlattice along the cross-plane direction by time-domain thermal reflectance (TDTR) method. The total κ could be suppressed to ~ 3.3 W m⁻¹ K⁻¹, similar to the minimum value of CaTiO₃/SrTiO₃-based superlattices ($\kappa \sim 3.2$ W m⁻¹ K⁻¹) reported by Ravichandran et al.²⁴. From these results, we judged that our [N uc SrTi_{1-x}Nb_xO₃][11 uc SrTiO₃]₁₀ superlattices (N is ranging from 1 to 12, x is ranging from 0.2 to 0.9) are appropriate for us to clarify the effectiveness of 2DES to enhance PF.

Thermoelectric properties. The electrical conductivity (σ), carrier concentration (n), and Hall mobility (μ_{Hall}) of the superlattices were measured at room temperature by a conventional d.c. four-probe method with a van der Pauw geometry. S was measured at room temperature by creating a temperature difference (ΔT) of ~ 4 K across the film using two Peltier devices. Figure 4a summarizes the n -dependent S of [N uc SrTi_{1-x}Nb_xO₃][11 uc SrTiO₃]₁₀ superlattices (N is ranging from 1 to 12, $x = 0.2, 0.3$, and 0.8) along with bulk (~ 100 -nm-thick SrTi_{1-x}Nb_xO₃ films, $x = 0.2, 0.3$, and 0.8 , respectively) values for comparison. The bulk S for $x = 0.2$ was -143 $\mu\text{V K}^{-1}$, $x = 0.3$ was -73 $\mu\text{V K}^{-1}$, and $x = 0.8$ was -19 $\mu\text{V K}^{-1}$. The n value was measured based on the total thickness of the 2DES, which includes the insulating SrTiO₃ layers. All the 2DES samples show enhanced thermopower ($-S$) with a reduced N . Compared to the bulk samples at a similar n , a much higher $-S$ is observed in superlattices as N is reduced below 3 uc.

To confirm the increasing two-dimensionality with x , the S -enhancement factors ($S_{2\text{DES}}/S_{\text{Bulk}}$) were plotted versus the N values (Fig. 4b). For 2DES with $x = 0.2$ and 0.3 , the highest $S_{2\text{DES}}/S_{\text{Bulk}}$ values are around 4 and 5, respectively, whereas that for the $x = 0.8$ counterpart is ~ 10 . As hypothesized, the enhanced $S_{2\text{DES}}/S_{\text{Bulk}}$ should stem from the increasing λ_D with x . In our experiment, $S_{2\text{DES}}/S_{\text{Bulk}}$ for the $x = 0.2$ and 0.3 2DESs are saturated around 11 uc, which is consistent with λ_D in region A (~ 4.2 nm indicated by dashed line $\lambda_{D,A}$). As λ_D increases in region B, the saturation position for the $x = 0.8$ 2DES has a thickness larger than the λ_D (~ 5.2 nm indicated by dashed line $\lambda_{D,B}$). As a result, a significantly enhanced two-dimensionality is achieved in the $x > 0.3$ region B, which fits well with our hypothesis and suggests that region B has the potential to further enhance the thermoelectric PF.

Based on the conclusions above, we have enhanced the thermoelectric PF in [1 uc SrTi_{1-x}Nb_xO₃][11 uc SrTiO₃]₁₀ superlattices by adjusting x between 0.2 and 0.9. Figure 5 summarizes the n dependences of the thermoelectric properties of [1 uc SrTi_{1-x}Nb_xO₃][11 uc SrTiO₃]₁₀ superlattices at room temperature along with the reported bulk values for comparison¹⁹. Following the bulk values, σ increases almost linearly with n (Fig. 5a), indicating that n dominates σ . In the SrTi_{1-x}Nb_xO₃ system, carriers are mostly due to Nb substitution. The high n also induces a highly Nb substituted region with a superiority in σ . However, σ for the superlattices remains lower than the bulk value due to the coexistence of 11 uc SrTiO₃ insulating layers.

μ_{Hall} for lower x of 2DESs ($x \leq 0.5$) fluctuates around $3\text{--}5$ cm² V⁻¹ s⁻¹, while for higher x 2DESs ($x \geq 0.6$) values are ~ 6 cm² V⁻¹ s⁻¹ (Fig. 5b). Usually, μ_{Hall} is controlled by the conduction band of materials along with the effects of crystal defects such as impurities and grain boundaries. In the bulk samples, μ_{Hall} sharply increases due to the transition of the conduction band from Ti 3d to Nb 4d as x increases into the highly Nb substituted region¹⁹. This pattern is also observed in

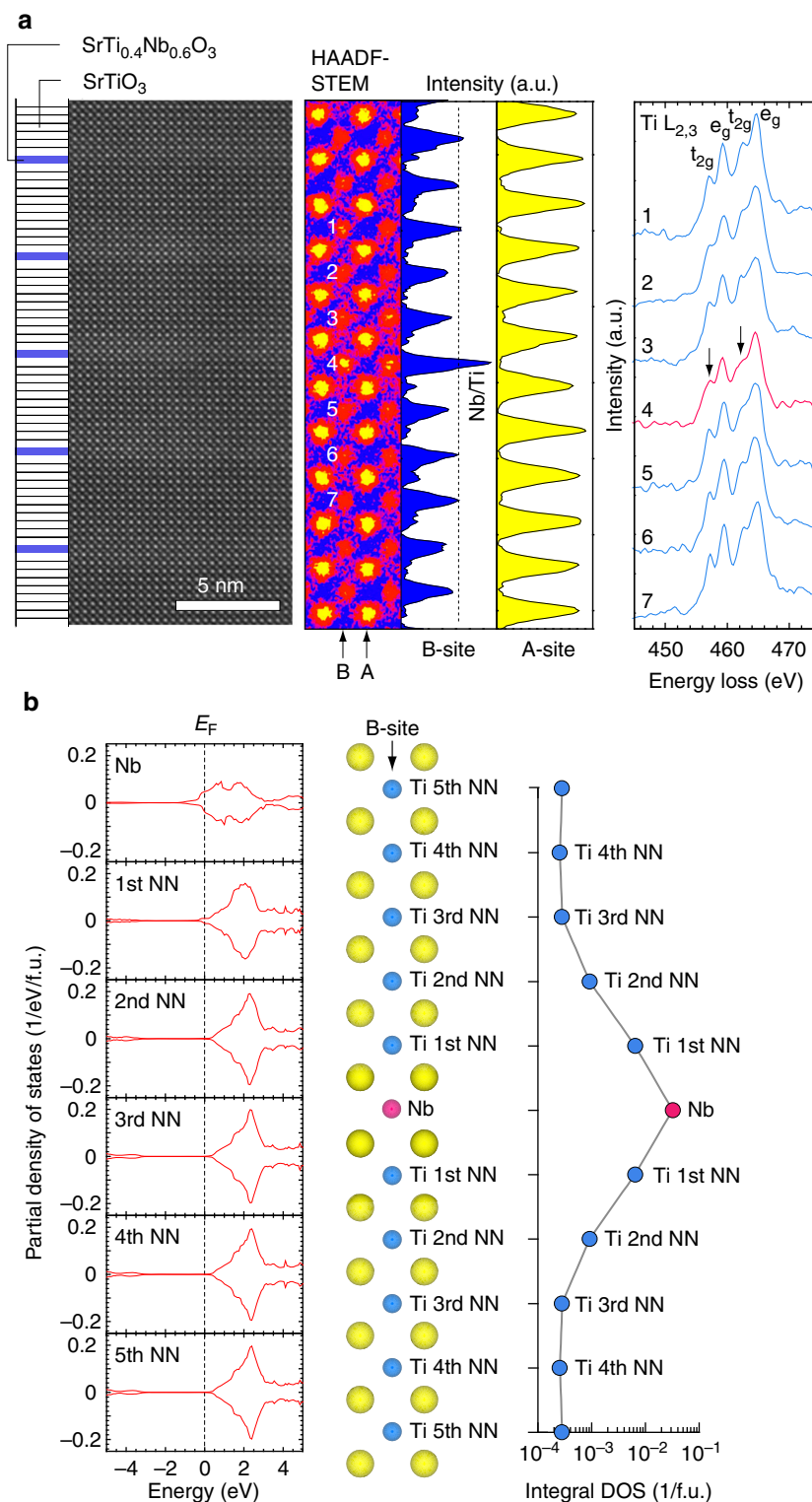


Fig. 3 Experimental and theoretical analyses of the 2DES. **a** Cross-sectional HAADF-STEM image of the [1 uc SrTi_{0.4}Nb_{0.6}O₃]₁₀ uc SrTiO₃ superlattice. Layer stacking sequence is also shown. Rather bright bands are seen near each SrTi_{0.4}Nb_{0.6}O₃ layer. In the magnified image, the #4 atom in the B-site column is brighter than the nearby atoms, whereas no obvious difference is observed in the A-site column. EELS spectrum of #4 is broader than that of nearby atoms, indicating the coexistence of Ti⁴⁺/Ti³⁺ in the SrTi_{0.4}Nb_{0.6}O₃ layers. **b** The calculated partial DOS of Nb 4d or Ti 3d in the [1 uc SrNbO₃]₁₀ uc SrTiO₃ superlattice. The Fermi energy (E_F) is located on the higher-energy side of the conduction band minimum for the first and second nearest neighbor (Ti first NN and Ti second NN). SrTiO₃ layers together with 1 uc SrNbO₃ layer (Nb) suggest that the electron carriers can see from the SrTi_{1-x}Nb_xO₃ layers into the SrTiO₃ layers

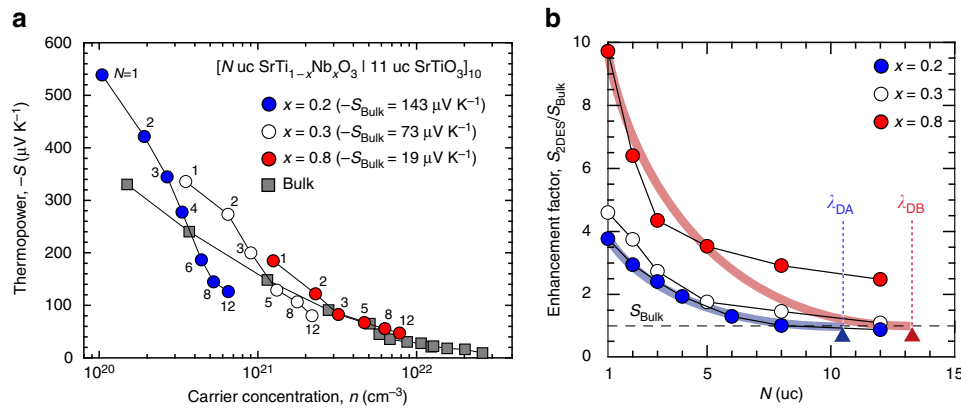


Fig. 4 Two-dimensionality of 2DES: a key to enhance thermopower. **a** Plots of thermopower of the 2DESs, $[N \text{ uc SrTi}_{1-x}\text{Nb}_x\text{O}_3 | 11 \text{ uc SrTiO}_3]_{10}$ superlattices ($x = 0.2, 0.3$, and 0.8), versus the carrier concentration (n). Compared to bulk values (gray squares), all the 2DESs show an enhanced $-S$ as N is reduced under 3 uc. **b** Enhancement factors in $-S$ (S_{2DES}/S_{Bulk}) for three sets of 2DESs. For $x = 0.2$ and 0.3 2DESs, the highest S_{2DES}/S_{Bulk} values are obtained at $N = 1$, which are 4 and 5, respectively, while that of $x = 0.8$ can reach 10

the superlattice counterparts. A higher μ_{Hall} ($\geq 6 \text{ cm}^2 \text{ V}^{-1} \text{ s}^{-1}$) is observed in samples with $x \geq 0.6$ than that for $x \leq 0.5$ ($3\text{--}5 \text{ cm}^2 \text{ V}^{-1} \text{ s}^{-1}$). Compared to the bulk samples, all the superlattices exert a much lower μ_{Hall} , which may result from an insufficient crystal quality or electron diffusion into the pure SrTiO_3 barrier layers. Regardless, a conduction band transition from $\text{Ti } 3d$ to $\text{Nb } 4d$ is recognized in our superlattice systems. Due to the high overlapping population of the $\text{Nb } 4d$ orbital, a superior electron transport property is realized in higher x of 2DES.

Figure 5c plots the S values for all the superlattices versus n along with the reported bulk values¹⁹. The solid line depicts the overall tendency. In the diagram, the superlattices have a significantly enhanced $-S$ compared to bulk samples at similar n values. As indicated by the solid lines, the experimental points for 2DES and bulk show different slopes of -300 and $-200 \text{ } \mu\text{V K}^{-1}$ per decade, respectively. The relationship between $-S$ and n_{eff} can be expressed by Eq. (3)

$$-S = -k_B/e \cdot \ln 10 \cdot A \cdot (\log n + B), \quad (3)$$

where k_B is the Boltzmann constant and e is an electron charge. A and B are the parameters that depend on the type of materials and their electronic band structures. Bulk shows a 3D electronic band structure with a parabolic shaped DOS near E_F , where the A value = 1 and the slope reflects a constant value of $-k_B/e \cdot \ln 10$ ($-198 \text{ } \mu\text{V K}^{-1}$). On the other hand, the slope of the 2DESs may reach $-300 \text{ } \mu\text{V K}^{-1}$ per decade, indicating that the A value = 1.5. Therefore, the 2DESs work well to enhance the S even for the whole superlattice, including SrTiO_3 insulating layers.

Finally, we calculated PF of the $[1 \text{ uc SrTi}_{1-x}\text{Nb}_x\text{O}_3 | 11 \text{ uc SrTiO}_3]_{10}$ superlattices (x is ranging from 0.2 to 0.9) using the observed S and σ values (Fig. 5d). PF is doubly enhanced for $x = 0.6$ ($5.1 \text{ mW m}^{-1} \text{ K}^{-2}$ at $n \sim 8 \times 10^{20} \text{ cm}^{-3}$). Since the PF values are scattered due to the rather large distribution of μ_{Hall} ($3\text{--}6 \text{ cm}^2 \text{ V}^{-1} \text{ s}^{-1}$), we calculated PFs using the relationship between S and n (c) at constant μ_{Hall} ($6 \text{ cm}^2 \text{ V}^{-1} \text{ s}^{-1}$). The optimized PF of the 2DES should be $\sim 5 \text{ mW m}^{-1} \text{ K}^{-2}$ at $n \sim 8 \times 10^{20} \text{ cm}^{-3}$, which doubles that of bulk $\text{SrTi}_{1-x}\text{Nb}_x\text{O}_3$ (PF $\sim 2.5 \text{ mW m}^{-1} \text{ K}^{-2}$ at $n \sim 2 \times 10^{21} \text{ cm}^{-3}$).

Discussion

The present 2DES, $[1 \text{ uc SrTi}_{1-x}\text{Nb}_x\text{O}_3 | 11 \text{ uc SrTiO}_3]_{10}$ superlattices (x is ranging from 0.2 to 0.9), has several merits to enhance PF as compared with other 2DESs such as $\text{PbTe/Pb}_{1-x}\text{Eu}_x\text{Te}$ multiple-quantum-well¹⁰, SiGe -based superlattices^{16,17}, and Bi_2Te_3 -based

superlattices¹⁸, which are already commercialized thermoelectric materials. This is because $\text{SrTi}_{1-x}\text{Nb}_x\text{O}_3$ can be deposited with 1 uc layer accuracy by PLD. Therefore, we can easily reduce the 2DEG thickness to $\sim 0.4 \text{ nm}$ (1 uc layer). Further, there are two different λ_D in $\text{SrTi}_{1-x}\text{Nb}_x\text{O}_3$; $\sim 4.1 \text{ nm}$ in the low conducting region and $\sim 5.3 \text{ nm}$ in the high conducting region. For enhancing PF, both S and σ play important roles. The present research implies that high conducting region is effective to enhance the thermoelectric PF in the 2DES. Herein highly Nb substitution are revealed to have the coexistence of both a high electron transport (high n and μ_{Hall}) and a high two-dimensionality (large λ_D).

In summary, we have experimentally clarified that an enhanced two-dimensionality of 2DES is efficient to improve thermoelectric PF. We measured the thermoelectric properties of 2DESs $[N \text{ uc SrTi}_{1-x}\text{Nb}_x\text{O}_3 | 11 \text{ uc SrTiO}_3]_{10}$ superlattices (N is ranging from 1 to 12, x is ranging from 0.2 to 0.9) because there are two different λ_D in this 2DES ($x > 0.3$: $\lambda_D \sim 5.3 \text{ nm}$; $x < 0.3$: $\lambda_D \sim 4.1 \text{ nm}$). The S -enhancement factor S_{2DES}/S_{Bulk} of the 2DES ($N = 1$) for $x > 0.3$ were ~ 10 , whereas those for $x < 0.3$ were 4–5. Maximum PF of the 2DES ($N = 1$, $x = 0.6$) exceeded $\sim 5 \text{ mW m}^{-1} \text{ K}^{-2}$, which doubles the value of optimized bulk $\text{SrTi}_{1-x}\text{Nb}_x\text{O}_3$ (PF $\sim 2.5 \text{ mW m}^{-1} \text{ K}^{-2}$). The present 2DES approach—use of longer λ_D —is epoch-making and is fruitful to design good thermoelectric materials showing high PF.

Methods

Fabrication and analyses of the 2DESs. A series of superlattices with the chemical formula of $[N \text{ uc SrTi}_{1-x}\text{Nb}_x\text{O}_3 | 11 \text{ uc SrTiO}_3]_{10}$ (N is ranging from 1 to 12, x is ranging from 0.2 to 0.9) were fabricated by a PLD technique using dense ceramic disks of a SrTiO_3 - SrNbO_3 mixture and a SrTiO_3 single crystal as the targets. The substrate was insulating (001) LaAlO_3 (pseudo-cubic perovskite, lattice parameter, a is 3.79 \AA , the surface area: $1 \text{ cm} \times 1 \text{ cm}$). The growth conditions were precisely controlled; the substrate temperature was $900 \text{ }^\circ\text{C}$, the oxygen pressure was $\sim 10^{-4} \text{ Pa}$, and the laser fluence was $\sim 1.2 \text{ J cm}^{-2}$ per pulse. The thicknesses of different layers were monitored in situ using the intensity oscillation of the RHEED spots. Details of our PLD growth process of the superlattices are reported elsewhere^{14,25}.

Crystallographic analyses of the resultant superlattices were performed by XRD (Cu $\text{K}\alpha_1$, ATX-G, Rigaku Co.), AFM (Nanocute, Hitachi Hi-Tech), and STEM (200 keV, JEM-ARM 200CF, JEOL Co. Ltd). TEM samples were fabricated using a cryo ion slicer (IB-09060CIS, JEOL Co. Ltd). HAADF images were taken with the detection angle of $68\text{--}280 \text{ mrad}$. Electron energy loss spectra were acquired in STEM mode with the energy resolution of 0.8 eV .

Measurements of the thermoelectric properties of the 2DESs. Electrical conductivity (σ), carrier concentration (n), and Hall mobility (μ_{Hall}) were measured at room temperature by a conventional d.c. four-probe method with a van der Pauw geometry. S was measured at room temperature by creating a temperature difference (ΔT) of $\sim 4 \text{ K}$ across the film using two Peltier devices. (Two small

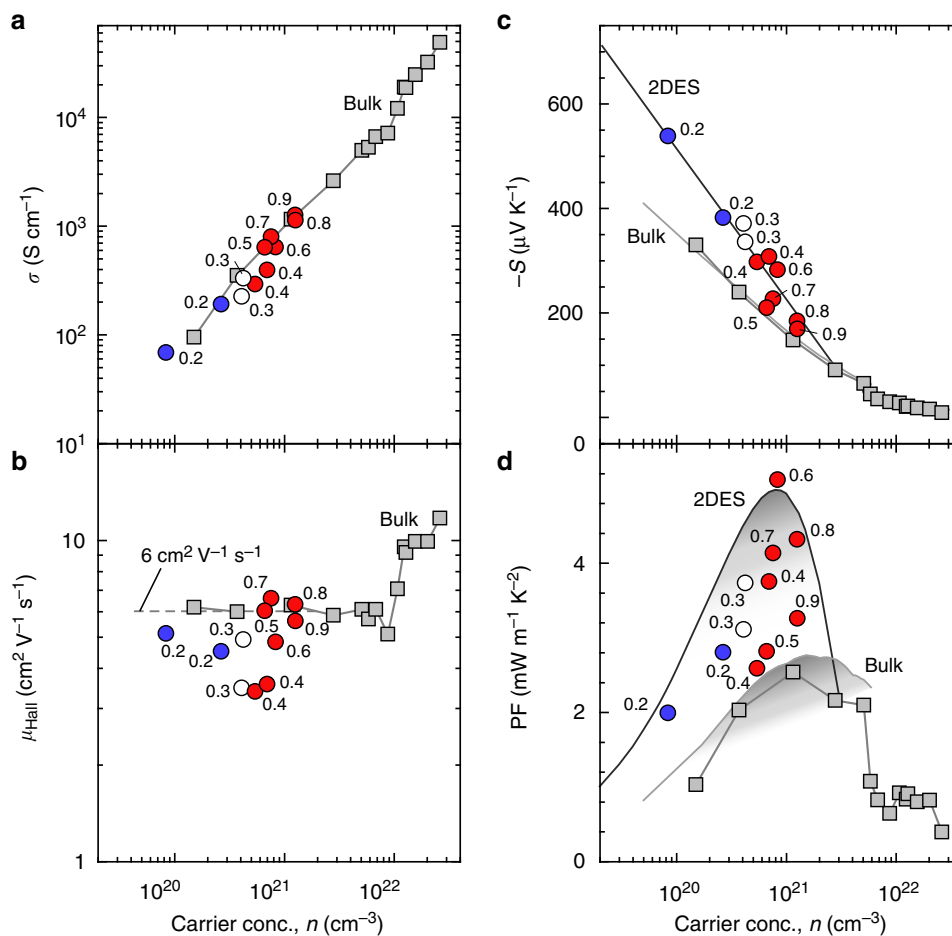


Fig. 5 Double enhancement of the thermoelectric power factor in a 2DES. Carrier concentration dependences of **a** electrical conductivity (σ), **b** Hall mobility (μ_{Hall}), **c** thermopower ($-S$), and **d** power factor [PF ($S^2\sigma$)] of [1 uc $\text{SrTi}_{1-x}\text{Nb}_x\text{O}_3$ | 11 uc SrTiO_3] $_{10}$ 2DESs (x is ranging from 0.2 to 0.9) at room temperature. Similar to the trends in the bulk values, σ increases almost linearly with n . μ_{Hall} for lower x samples ($x \leq 0.5$) fluctuates around $3-5 \text{ cm}^2 \text{V}^{-1} \text{s}^{-1}$, while that for higher x ones ($x \geq 0.6$) is $\sim 6 \text{ cm}^2 \text{V}^{-1} \text{s}^{-1}$. Slope of $-S$ versus $\log n$ for bulk $\text{SrTi}_{1-x}\text{Nb}_x\text{O}_3$ is $\sim -198 \mu\text{V K}^{-1}$, which is ~ 1.5 times lower than $\sim -300 \mu\text{V K}^{-1}$ for the 2DESs. Double enhancement of PF is seen in $x = 0.6$ ($5.1 \text{ mW m}^{-1} \text{K}^{-2}$ at $n \sim 8 \times 10^{20} \text{ cm}^{-3}$). Since the PF values are scattered due to the rather large distribution of μ_{Hall} ($3-6 \text{ cm}^2 \text{V}^{-1} \text{s}^{-1}$), we calculated PFs using the relationship between S and n (c) at constant μ_{Hall} ($6 \text{ cm}^2 \text{V}^{-1} \text{s}^{-1}$). The optimized PF of the 2DES should be $\sim 5 \text{ mW m}^{-1} \text{K}^{-2}$ at $n \sim 8 \times 10^{20} \text{ cm}^{-3}$, which doubles that of bulk $\text{SrTi}_{1-x}\text{Nb}_x\text{O}_3$ (PF $\sim 2.5 \text{ mW m}^{-1} \text{K}^{-2}$ at $n \sim 2 \times 10^{21} \text{ cm}^{-3}$)

thermocouples were used to monitor the actual temperatures of each end of a superlattice.) The thermo-electromotive force (ΔV) and ΔT were measured simultaneously, and the S values were obtained from the slope of the $\Delta V-\Delta T$ plots (the correlation coefficient: >0.9999).

Cross-plane thermal conductivity (κ) was measured by TDTR (Picotherm Co.) method. Mode-locked fiber pulse lasers with 1550 and 775 nm wavelengths were used for heating and measuring, respectively. Both lasers are with the repetition frequency of 20 MHz and pulse duration of 0.4 ps. Before measurement, Mo film with a thickness of 100 nm was first deposited on the surface of the sample as the transducer. During measurement, time-dependent transient thermoreflectance phase signal of Mo transducer was measured, from which κ was further simulated. Time-domain thermoreflectance was measured based on amplified laser systems (5 kHz and ~ 200 fs centered at 1030 nm). Degenerate pump and probe photons were separated by the cross polarization, and a polarizing filter was employed before the lock-in detection. A mechanical delay stage was used for time scan up to 1.5 ns. Pump to probe intensity ratio was >15 , and the size ratio was around 6.

Energy band calculation of the 2DES. Band structure for the [1 uc SrNbO_3 | 10 uc SrTiO_3] superlattice was calculated based on the PAW method²⁶, as implemented in the VASP code^{27,28}. We adopted the Heyd-Scuseria-Ernzerhof hybrid functionals²⁹⁻³¹ and a plane-wave cutoff energy of 550 eV. $6 \times 6 \times 6$ and $6 \times 6 \times 2$ k -point meshes were employed in the total-energy evaluations and geometry optimization for the perovskite unit cells of SrTiO_3 and the superlattice cell, respectively. The in-plane lattice constant of the superlattice cell was fixed at the optimized value of SrTiO_3 while the out-of-plane lattice constant and the atomic coordinates were fully relaxed.

Data availability. The data that support the findings of this study are available from the corresponding authors upon reasonable request.

Received: 28 January 2018 Accepted: 16 May 2018

Published online: 20 June 2018

References

- DiSalvo, F. J. Thermoelectric cooling and power generation. *Science* **285**, 703–706 (1999).
- Snyder, G. J. & Toberer, E. S. Complex thermoelectric materials. *Nat. Mater.* **7**, 105–114 (2008).
- Vining, C. B. An inconvenient truth about thermoelectrics. *Nat. Mater.* **8**, 83–85 (2009).
- Zhang, Q. H. et al. Thermoelectric devices for power generation: recent progress and future challenges. *Adv. Eng. Mater.* **18**, 194–213 (2016).
- Hsu, K. F. et al. Cubic $\text{AgPb}_m\text{SbTe}_{2+m}$: bulk thermoelectric materials with high figure of merit. *Science* **303**, 818–821 (2004).
- Poudel, B. et al. High-thermoelectric performance of nanostructured bismuth antimony telluride bulk alloys. *Science* **320**, 634–638 (2008).
- Il Kim, S. et al. Dense dislocation arrays embedded in grain boundaries for high-performance bulk thermoelectrics. *Science* **348**, 109–114 (2015).
- Biswas, K. et al. High-performance bulk thermoelectrics with all-scale hierarchical architectures. *Nature* **489**, 414–418 (2012).

9. Hicks, L. D. & Dresselhaus, M. S. Effect of quantum-well structures on the thermoelectric figure of merit. *Phys. Rev. B* **47**, 12727–12731 (1993).
10. Hicks, L. D., Harman, T. C., Sun, X. & Dresselhaus, M. S. Experimental study of the effect of quantum-well structures on the thermoelectric figure of merit. *Phys. Rev. B* **53**, 10493–10496 (1996).
11. Hung, N. T., Hasdeo, E. H., Nugraha, A. R. T., Dresselhaus, M. S. & Saito, R. Quantum effects in the thermoelectric power factor of low-dimensional semiconductors. *Phys. Rev. Lett.* **117**, 036602 (2016).
12. Mao, J., Liu, Z. H. & Ren, Z. F. Size effect in thermoelectric materials. *npj Quantum Mater.* **1**, 16028 (2016).
13. Hung, N. T., Nugraha, A. R. T. & Saito, R. Two-dimensional InSe as a potential thermoelectric material. *Appl. Phys. Lett.* **111**, 092107 (2017).
14. Ohta, H. et al. Giant thermoelectric Seebeck coefficient of two-dimensional electron gas in SrTiO₃. *Nat. Mater.* **6**, 129–134 (2007).
15. Choi, W. S., Ohta, H. & Lee, H. N. Thermopower enhancement by fractional layer control in 2D oxide superlattices. *Adv. Mater.* **26**, 6701–6705 (2014).
16. Koga, T., Cronin, S. B., Dresselhaus, M. S., Liu, J. L. & Wang, K. L. Experimental proof-of-principle investigation of enhanced Z(3D)T in (001) oriented Si/Ge superlattices. *Appl. Phys. Lett.* **77**, 1490–1492 (2000).
17. Samarelli, A. et al. The thermoelectric properties of Ge/SiGe modulation doped superlattices. *J. Appl. Phys.* **113**, 233704 (2013).
18. Peranio, N., Eibl, O. & Nurnus, J. Structural and thermoelectric properties of epitaxially grown Bi₂Te₃ thin films and superlattices. *J. Appl. Phys.* **100**, 114306 (2006).
19. Zhang, Y. et al. Thermoelectric phase diagram of the SrTiO₃-SrNbO₃ solid solution system. *J. Appl. Phys.* **121**, 185102 (2017).
20. Shannon, R. D. Revised effective ionic radii and systematic studies of interatomic distances in halides and chalcogenides. *Acta Crystallogr. A* **32**, 751–767 (1976).
21. Ohtomo, A., Muller, D. A., Grazul, J. L. & Hwang, H. Y. Artificial charge-modulation in atomic-scale perovskite titanate superlattices. *Nature* **419**, 378–380 (2002).
22. Mizoguchi, T., Ohta, H., Lee, H. S., Takahashi, N. & Ikuhara, Y. Controlling interface intermixing and properties of SrTiO₃-based superlattices. *Adv. Funct. Mater.* **21**, 2258–2263 (2011).
23. Delugas, P. et al. Doping-induced dimensional crossover and thermopower burst in Nb-doped SrTiO₃ superlattices. *Phys. Rev. B* **88**, 045310 (2013).
24. Ravichandran, J. et al. Crossover from incoherent to coherent phonon scattering in epitaxial oxide superlattices. *Nat. Mater.* **13**, 168–172 (2014).
25. Mune, Y., Ohta, H., Koumoto, K., Mizoguchi, T. & Ikuhara, Y. Enhanced Seebeck coefficient of quantum-confined electrons in SrTiO₃/SrTi_{0.8}Nb_{0.2}O₃ superlattices. *Appl. Phys. Lett.* **91**, 192105 (2007).
26. Blochl, P. E. Projector augmented-wave method. *Phys. Rev. B* **50**, 17953–17979 (1994).
27. Kresse, G. & Joubert, D. From ultrasoft pseudopotentials to the projector augmented-wave method. *Phys. Rev. B* **59**, 1758–1775 (1999).
28. Kresse, G. & Furthmüller, J. Efficient iterative schemes for ab initio total-energy calculations using a plane-wave basis set. *Phys. Rev. B* **54**, 11169–11186 (1996).
29. Heyd, J., Scuseria, G. E. & Ernzerhof, M. Hybrid functionals based on a screened Coulomb potential. *J. Chem. Phys.* **124**, 219906 (2006).
30. Krukau, A. V., Vydrov, O. A., Izmaylov, A. F. & Scuseria, G. E. Influence of the exchange screening parameter on the performance of screened hybrid functionals. *J. Chem. Phys.* **125**, 224106 (2006).
31. Heyd, J., Scuseria, G. E. & Ernzerhof, M. Hybrid functionals based on a screened Coulomb potential. *J. Chem. Phys.* **118**, 8207–8215 (2003).

Acknowledgements

This research was supported by Grants-in-Aid for Scientific Research on Innovative Areas “Nano Informatics” (25106003, 25106005, and 25106007) from the Japan Society for the Promotion of Science (JSPS). H.O. was supported by Grants-in-Aid for Scientific Research A (17H01314) and B (26287064) from the JSPS. Y.Z. thanks to the China Scholarship Council (CSC) for a scholarship to study in Japan. Y.M.S. acknowledge the grant from Taiwan Ministry of Science and Technology (MOST 104-2112-M-009-023-MY3 and MOST 104-2738-M-009-006), and the Center for Emergent Functional Matter Science of National Chiao Tung University from The Featured Areas Research Center Program within the framework of the Higher Education Sprout Project by the Ministry of Education (MOE) in Taiwan. A part of this work was supported in part by the Network Joint Research Center for Materials and Devices and by Dynamic Alliance for Open Innovation Bridging Human, Environment and Materials.

Author contributions

Y.Z. performed the sample preparation and measurements. B.F. and Y.I. performed the STEM analyses. H.H. and I.T. performed the energy band calculations. C.P.C. and Y.M.S. provided measurements on the time-domain thermoreflectance. H.O. planned and supervised the project. All authors discussed the results and commented on the manuscript.

Additional information

Supplementary Information accompanies this paper at <https://doi.org/10.1038/s41467-018-04660-4>.

Competing interests: The authors declare no competing interests.

Reprints and permission information is available online at <http://npg.nature.com/reprintsandpermissions/>

Publisher's note: Springer Nature remains neutral with regard to jurisdictional claims in published maps and institutional affiliations.



Open Access This article is licensed under a Creative Commons Attribution 4.0 International License, which permits use, sharing, adaptation, distribution and reproduction in any medium or format, as long as you give appropriate credit to the original author(s) and the source, provide a link to the Creative Commons license, and indicate if changes were made. The images or other third party material in this article are included in the article's Creative Commons license, unless indicated otherwise in a credit line to the material. If material is not included in the article's Creative Commons license and your intended use is not permitted by statutory regulation or exceeds the permitted use, you will need to obtain permission directly from the copyright holder. To view a copy of this license, visit <http://creativecommons.org/licenses/by/4.0/>.

© The Author(s) 2018